We are IntechOpen,
the world's leading publisher of
Open Access books
Built by scientists, for scientists

4,800
Open access books available

122,000
International authors and editors

135M
Downloads

Our authors are among the

154
Countries delivered to

TOP 1%
most cited scientists

12.2%
Contributors from top 500 universities

CLARIVATE ANALYTICS
BOOK
CITATION
INDEX
INDEXED

WEB OF SCIENCE™

Selection of our books indexed in the Book Citation Index
in Web of Science™ Core Collection (BKCI)

Interested in publishing with us?
Contact book.department@intechopen.com

A Microscopic Equation of State for Neutron-Rich Matter and Its Effect on Neutron Star Properties

Francesca Sammarruca
University of Idaho
USA

1. Introduction

In this chapter, we will be concerned with hadronic interactions in the nuclear medium, particularly under conditions of extreme densities such as those encountered in some compact astrophysical objects. This issue goes to the very core of nuclear physics. In fact, our present knowledge of the nuclear force in free space is, in itself, the result of decades of struggle (Machleidt, 1989) which will not be reviewed in this chapter. The nature of the nuclear force in the medium is of course an even more complex problem, as it involves aspects of the force that cannot be constrained through free-space nucleon-nucleon (NN) scattering. Predictions of properties of nuclei are the ultimate test for many-body theories.

Nuclear matter is a convenient theoretical laboratory for many-body theories. By "nuclear matter" we mean an infinite system of nucleons acted on by their mutual strong forces and no electromagnetic interactions. Nuclear matter is characterized by its energy per particle as a function of density and other thermodynamic quantities, as appropriate (e.g. temperature). Such relation is known as the nuclear matter equation of state (EoS). The translational invariance of the system facilitates theoretical calculations. At the same time, adopting what is known as the "local density approximation", one can use the EoS to obtain information on finite systems. This procedure is applied, for instance, in Thomas-Fermi calculations within the liquid drop model, where an appropriate energy functional is written in terms of the EoS (Furnstahl, 2002; Oyamatsu et al., 1998; Sammarruca & Liu, 2009).

Isospin-asymmetric nuclear matter (IANM) simulates the interior of a nucleus with unequal densities of protons and neutrons. The equation of state of (cold) IANM is then a function of density as well as the relative concentrations of protons and neutrons.

The recent and fast-growing interest in IANM stems from its close connection to the physics of neutron-rich nuclei, or, more generally, isospin-asymmetric nuclei, including the very "exotic" ones known as "halo" nuclei. At this time, the boundaries of the nuclear chart are uncertain, with several thousands nuclei believed to exist but not yet observed in terrestrial laboratories. The Facility for Rare Isotope Beams (FRIB) has recently been approved for design and construction at Michigan State University. The facility will deliver intense beams of rare isotopes, the study of which can provide crucial information on short-lived elements normally not found on earth. Thus, this new experimental program will have widespread impact, ranging from the origin of elements to the evolution of the cosmos. It is estimated

that the design and construction of FRIB will take ten years. In the meantime, systematic investigations to determine the properties of asymmetric nuclear matter are proliferating at existing facilities.

The equation of state of IANM is also the crucial input for the structure equations of compact stars, and thus establishes the connection between nuclear physics and compact astrophysical systems. It is the focal point of this chapter to present and discuss our approach to the devolopment of the EoS of nuclear and neutron-rich matter, with particular emphasis on the latter and its relation to the properties of neutron stars.

The chapter will articulate through the following sections: In Section **2**, we present a brief review of facts and phenomenology about IANM. We then proceed to describe our microscopic approach to calculate the energy per particle in IANM (Section **3**) and show the corresponding predictions. Section **4** will be dedicated to a review of neutron star structure and available empirical constraints. Microscopic predictions of neutron star properties will be presented and discussed there. Section **5** contains a brief discussion on the topic of polarized IANM. The chapter will end with our conclusions and an outlook into the future (Section **6**).

2. Facts about isospin-asymmetric nuclear matter

Asymmetric nuclear matter can be characterized by the neutron density, ρ_n, and the proton density, ρ_p, defined as the number of neutrons or protons per unit of volume. In infinite matter, they are obtained by summing the neutron or proton states per volume (up to their respective Fermi momenta, k_F^n or k_F^p) and applying the appropriate degeneracy factor. The result is

$$\rho_i = \frac{(k_F^i)^3}{3\pi^2},\tag{1}$$

with $i = n$ or p.

It may be more convenient to refer to the total density $\rho = \rho_n + \rho_p$ and the asymmetry (or neutron excess) parameter $\alpha = \frac{\rho_n - \rho_p}{\rho}$. Clearly, α=0 corresponds to symmetric matter and α=1 to neutron matter. In terms of α and the average Fermi momentum, k_F, related to the total density in the usual way,

$$\rho = \frac{2k_F^3}{3\pi^2},\tag{2}$$

the neutron and proton Fermi momenta can be expressed as

$$k_F^n = k_F(1+\alpha)^{1/3}\tag{3}$$

and

$$k_F^p = k_F(1-\alpha)^{1/3},\tag{4}$$

respectively.

Expanding the energy per particle in IANM with respect to the asymmetry parameter yields

$$e(\rho,\alpha) = e_0(\rho) + \frac{1}{2}\left(\frac{\partial^2 e(\rho,\alpha)}{\partial\alpha^2}\right)_{\alpha=0}\alpha^2 + \mathcal{O}(\alpha^4),\tag{5}$$

where the first term is the energy per particle in symmetric matter and the coefficient of the quadratic term is identified with the symmetry energy, e_{sym}. In the Bethe-Weizsäcker formula for the nuclear binding energy, it represents the amount of binding a nucleus has to lose when the numbers of protons and neutrons are unequal. A typical value for e_{sym} at nuclear matter density (ρ_0) is 30 MeV, with theoretical predictions spreading approximately between 26 and 35 MeV.

To a very good degree of approximation, the energy per particle in IANM can be written as

$$e(\rho, \alpha) \approx e_0(\rho) + e_{sym}(\rho)\alpha^2. \tag{6}$$

The effect of a term of fourth order in the asymmetry parameter ($\mathcal{O}(\alpha^4)$) on the bulk properties of neutron stars is very small, although it may impact the proton fraction at high density.

Equation (6) displays a convenient separation between the symmetric and aymmetric parts of the EoS, which facilitates the identification of observables that may be sensitive, for instance, mainly to the symmetry energy. At this time, groups from GSI (Sfienti et al., 2009; Trautmann et al., 2009), MSU (Tsang et al., 2009), Italy (Greco, 2010), France (Borderie & Rivet, 2008), China (Feng, 2010; Yong, 2010), Japan (Isobe, 2011), Texas A&M (Kohley et al., 2011), and more are investigating the density dependence of the symmetry energy through heavy-ion collisions. Typically, constraints are extracted from heavy-ion collision simulations based on transport models. Isospin diffusion and the ratio of neutron and proton spectra are among the observables used in these analyses.

These investigations appear to agree reasonably well on the following parametrization of the symmetry energy:

$$e_{sym}(\rho) = 12.5\,MeV\left(\frac{\rho}{\rho_0}\right)^{2/3} + 17.5\,MeV\left(\frac{\rho}{\rho_0}\right)^{\gamma_i}, \tag{7}$$

where ρ_0 is the saturation density. The first term is the kinetic contribution and γ_i (the exponent appearing in the potential energy part) is found to be between 0.4 and 1.0. Recent measurements of elliptic flows in ^{197}Au + ^{197}Au reactions at GSI at 400-800 MeV per nucleon favor a potential energy term with γ_i equal to 0.9 ± 0.4. Giant dipole resonance excitation in fusion reactions (Simenel et al., 2007) is also sensitive to the symmetry energy, since the latter is responsible for isospin equilibration in isospin-asymmetric collisions.

Isospin-sensitive observables can also be identified among the properties of normal nuclei. The neutron skin of neutron-rich nuclei is a powerful isovector observable, being sensitive to the slope of the symmetry energy, which determines to which extent neutrons will tend to spread outwards to form the skin.

Parity-violating electron scattering experiments are now a realistic option to determine neutron distributions with unprecedented accuracy. The neutron radius of ^{208}Pb is expected to be measured with a precision of 3% thanks to the electroweak program at the Jefferson Laboratory, the PREX experiment in particular, just recently completed at Jefferson Lab. This level of accuracy could not be achieved with hadronic scattering. Parity-violating electron scattering at low momentum transfer is especially suitable to probe neutron densities, as the Z^0 boson couples primarily to neutrons. With the success of this program, reliable empirical

information on neutron skins will be able to provide, in turn, much needed *independent* constraint on the density dependence of the symmetry energy.

A measure of the density dependence of the symmetry energy is the symmetry pressure, closely related to the parameter

$$L = 3\rho_0 \left(\frac{\partial e_{sym}(\rho)}{\partial \rho} \right)_{\rho_0} \approx 3\rho_0 \left(\frac{\partial e_{n.m.}(\rho)}{\partial \rho} \right)_{\rho_0}, \tag{8}$$

where we have used Eq. (6) with α=1. Thus, L is sensitive to the gradient of the energy per particle in neutron matter ($e_{n.m.}$). As to be expected on physical grounds, the neutron skin, given by

$$S = \sqrt{<r_n^2>} - \sqrt{<r_p^2>}, \tag{9}$$

is highly sensitive to the same pressure gradient.

Values of L are reported to range from -50 to 100 MeV as seen, for instance, through the numerous parametrizations of Skyrme interactions, all chosen to fit the binding energies and the charge radii of a large number of nuclei, see (Li & Chen, 2005) and references therein. Heavy-ion data impose boundaries for L at 85 ± 25 MeV, with more stringent constraints being presently extracted. At this time constraints appear to favor lower values of L. . In fact, a range of L values given by 52.7 ± 22.5 MeV has emerged from recent analyses of global optical potentials (Xu et al., 2010).

Typically, parametrizations like the one given in Eq. (7) are valid at or below the saturation density, ρ_0. Efforts to constrain the behavior of the symmetry energy at higher densities are presently being pursued through observables such as π^-/π^+ ratio, K^+/K^0 ratio, neutron/proton differential transverse flow, or nucleon elliptic flow (Ko et al., 2010).

Another important quantity which emerges from studies of IANM is the symmetry potential. Its definition stems from the observation that the single-particle potentials experienced by the proton and the neutron in IANM, $U_{n/p}$, are different from each other and satisfy the approximate relation

$$U_{n/p}(k,\rho,\alpha) \approx U_{n/p}(k,\rho,\alpha=0) \pm U_{sym}(k,\rho)\, \alpha, \tag{10}$$

where the +(-) sign refers to neutrons (protons), and

$$U_{sym} = \frac{U_n - U_p}{2\alpha}. \tag{11}$$

(Later in the chapter we will verify the approximate linear behavior with respect to α displayed in Eq. (10).) Thus, one can expect isospin splitting of the single-particle potential to be effective in separating the collision dynamics of neutrons and protons. Furthermore, U_{sym}, being proportional to the gradient between the single-neutron and the single-proton potentials, should be comparable with the Lane potential (Lane, 1962), namely the isovector part of the nuclear optical potential. Optical potential analyses can then help constrain this quantity and, in turn, the symmetry energy.

Because of the fundamental importance of the symmetry energy in many systems and phenomena, it is of interest to identify the main contributions to its density dependence. In a recent work (Sammarruca, 2011) we discussed the contribution of the isovector mesons (π, ρ, and δ) to the symmetry energy and demonstrated the chief role of the pion. Note that the isovector mesons carry the isospin dependence by contributing differently in different partial waves, and that isospin dependence controls the physics of IANM. Hence, we stress the relevance of a microscopic model that contains all important couplings of mesons with nucleons.

3. Our microscopic approach to isospin-asymmetric nuclear matter

3.1 The two-body potential

Our approach is *ab initio* in that the starting point of the many-body calculation is a realistic NN interaction which is then applied in the nuclear medium without any additional free parameters. Thus the first question to be confronted concerns the choice of the "best" NN interaction. After the development of Quantum Chromodynamics (QCD) and the understanding of its symmetries, chiral effective theories (Weinberg, 1990) were developed as a way to respect the symmetries of QCD while keeping the degrees of freedom (nucleons and pions) typical of low-energy nuclear physics. However, chiral perturbation theory (ChPT) has definite limitations as far as the range of allowed momenta is concerned. For the purpose of applications in dense matter, where higher and higher momenta become involved with increasing Fermi momentum, NN potentials based on ChPT are unsuitable.

Relativistic meson theory is an appropriate framework to deal with the high momenta encountered in dense matter. In particular, the one-boson-exchange (OBE) model has proven very successful in describing NN data in free space and has a good theoretical foundation. Among the many available OBE potentials, some being part of the "high-precision generation" (Machleidt, 2001; Stocks et al., 1994; Wiringa et al., 1995), we seek a momentum-space potential developed within a relativistic scattering equation, such as the one obtained through the Thompson (Thompson, 1970) three-dimensional reduction of the Bethe-Salpeter equation (Salpeter & Bether, 1951). Furthermore, we require a potential that uses the pseudovector coupling for the interaction of nucleons with pseudoscalar mesons. With these constraints in mind, as well as the requirement of a good description of the NN data, Bonn B (Machleidt, 1989) is a reasonable choice. As is well known, the NN potential model dependence of nuclear matter predictions is not negligible. The saturation points obtained with different NN potentials move along the famous "Coester band" depending on the strength of the tensor force, with the weakest tensor force yielding the largest attraction. This can be understood in terms of medium effects (particularly Pauli blocking) reducing the (attractive) second-order term in the expansion of the reaction matrix. A large second-order term will undergo a large reduction in the medium. Therefore, noticing that the second-order term is dominated by the tensor component of the force, nuclear potentials with a strong tensor component will yield less attraction in the medium. For the same reason (that is, the role of the tensor force in nuclear matter), the potential model dependence is strongly reduced in pure (or nearly pure) neutron matter, due to the absence of isospin-zero partial waves.

Already when QCD (and its symmetries) were unknown, it was observed that the contribution from the nucleon-antinucleon pair diagram, Fig. 1, becomes unreasonably large if the
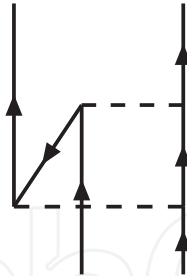
Fig. 1. Contribution to the NN interaction from virtual pair excitation. Upward- and downward-pointing arrows represent nucleons and antinucleons, respectively. Dashed lines denote mesons.
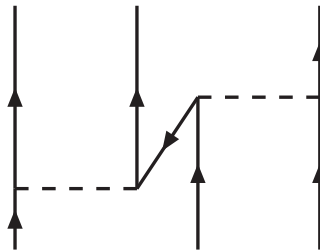

Fig. 2. Three-body force due to virtual pair excitation. Conventions as in the previous figure.

pseudoscalar (ps) coupling is used, leading to very large pion-nucleon scattering lengths (Brown, 1979). We recall that the Lagrangian density for pseudoscalar coupling of the nucleon field (ψ) with the pseudoscalar meson field (ϕ) is

$$\mathcal{L}_{ps} = -ig_{ps}\bar{\psi}\gamma_5\psi\phi. \tag{12}$$

On the other hand, the same contribution, shown in Fig. 1, is heavily reduced by the pseudovector (pv) coupling (a mechanism which became known as "pair suppression"). The reason for the suppression is the presence of the covariant derivative at the pseudovector vertex,

$$\mathcal{L}_{pv} = \frac{f_{ps}}{m_{ps}}\bar{\psi}\gamma_5\gamma^{\mu}\psi\partial_{\mu}\phi, \tag{13}$$

which reduces the contribution of the vertex for low momenta and, thus, explains the small value of the pion-nucleon scattering length at threshold (Brown, 1979). Considerations based on chiral symmetry (Brown, 1979) can further motivate the choice of the pseudovector coupling.

In closing this section, we wish to highlight the most important aspect of the *ab initio* approach: Namely, the only free parameters of the model (the parameters of the NN potential) are determined by fitting the free-space NN data and never readjusted in the medium. In other words, the model parameters are tightly constrained and the calculation in the medium is parameter free. The presence of free parameters in the medium would generate effects and sensitivities which are hard to control and interfere with the predictive power of the theory.

3.2 The Dirac-Brueckner-Hartree-Fock approach to symmetric and asymmetric nuclear matter

3.2.1 Formalism

The main strength of the DBHF approach is its inherent ability to account for important three-body forces through its density dependence. In Fig. 2 we show a three-body force (TBF) originating from virtual excitation of a nucleon-antinucleon pair, known as "Z-diagram". Notice that the observations from the previous section ensure that the corresponding diagram at the two-body level, Fig. 1, is moderate in size when the pv coupling, Eq. 13, is used. The main feature of the DBHF method turns out to be closely related to the TBF depicted in Fig. 2, as we will argue next. In the DBHF approach, one describes the positive energy solutions of the Dirac equation in the medium as

$$u^*(p, \lambda) = \left(\frac{E_p^* + m^*}{2m^*} \right)^{1/2} \left(\frac{\mathbf{1}}{\frac{\sigma \cdot \vec{p}}{E_p^* + m^*}} \right) \chi_\lambda, \tag{14}$$

where the nucleon effective mass, m^*, is defined as $m^* = m + U_S$, with U_S an attractive scalar potential. (This will be derived below.) It can be shown that both the description of a single-nucleon via Eq. (14) and the evaluation of the Z-diagram, Fig. 2, generate a repulsive effect on the energy per particle in symmetric nuclear matter which depends on the density approximately as

$$\Delta E \propto \left(\frac{\rho}{\rho_0} \right)^{8/3}, \tag{15}$$

and provides the saturating mechanism missing from conventional Brueckner calculations. (Alternatively, explicit TBF are used along with the BHF method in order to achieve a similar result.) Brown showed that the bulk of the desired effect can be obtained as a lowest order (in p^2/m) relativistic correction to the single-particle propagation (Brown et al., 1987). With the in-medium spinor as in Eq. (14), the correction to the free-space spinor can be written approximately as

$$u^*(p, \lambda) - u(p, \lambda) \approx \left(\frac{\mathbf{0}}{-\frac{\sigma \cdot \vec{p}}{2m^2} U_S} \right) \chi_\lambda, \tag{16}$$

where for simplicity the spinor normalization factor has been set equal to 1, in which case it is clearly seen that the entire effect originates from the modification of the spinor's lower component. By expanding the single-particle energy to order U_S^2, Brown showed that the correction to the energy consistent with Eq. (16) can be written as $\frac{p^2}{2m} \left(\frac{U_S}{m} \right)^2$. He then proceeded to estimate the correction to the energy per particle and found it to be approximately as given in Eq. (15).

The approximate equivalence of the effective-mass description of Dirac states and the contribution from the Z-diagram has a simple intuitive explanation in the observation that Eq. (14), like any other solution of the Dirac equation, can be written as a superposition of positive and negative energy solutions. On the other hand, the "nucleon" in the middle of the Z-diagram, Fig. 2, is precisely a superposition of positive and negative energy states. In

summary, the DBHF method effectively takes into account a particular class of TBF, which are crucial for nuclear matter saturation.

Having first summarized the main DBHF philosophy, we now proceed to describe the DBHF calculation of IANM (Alonso & Sammarruca, 2003; Sammarruca, 2010). In the end, this will take us back to the crucial point of the DBHF approximation, Eq. (14).

We start from the Thompson (Thompson, 1970) relativistic three-dimensional reduction of the Bethe-Salpeter equation (Salpeter & Bether, 1951). The Thompson equation is applied to nuclear matter in strict analogy to free-space scattering and reads, in the nuclear matter rest frame,

$$g_{ij}(\vec{q}', \vec{q}, \vec{P}, (\epsilon_{ij}^*)_0) = v_{ij}^*(\vec{q}', \vec{q})$$
$$+ \int \frac{d^3K}{(2\pi)^3} v_{ij}^*(\vec{q}', \vec{K}) \frac{m_i^* m_j^*}{E_i^* E_j^*} \frac{Q_{ij}(\vec{K}, \vec{P})}{(\epsilon_{ij}^*)_0 - \epsilon_{ij}^*(\vec{P}, \vec{K})} g_{ij}(\vec{K}, \vec{q}, \vec{P}, (\epsilon_{ij}^*)_0) , \qquad (17)$$

where g_{ij} is the in-medium reaction matrix ($ij=nn$, pp, or np), and the asterix signifies that medium effects are applied to those quantities. Thus the NN potential, v_{ij}^*, is constructed in terms of effective Dirac states (in-medium spinors) as explained above. In Eq. (17), $\vec{q}$, $\vec{q}'$, and $\vec{K}$ are the initial, final, and intermediate relative momenta, and $E_i^* = \sqrt{(m_i^*)^2 + K^2}$. The momenta of the two interacting particles in the nuclear matter rest frame have been expressed in terms of their relative momentum and the center-of-mass momentum, $\vec{P}$, through

$$\vec{P} = \vec{k}_1 + \vec{k}_2 \qquad (18)$$

and

$$\vec{K} = \frac{\vec{k}_1 - \vec{k}_2}{2} . \qquad (19)$$

The energy of the two-particle system is

$$\epsilon_{ij}^*(\vec{P}, \vec{K}) = e_i^*(\vec{P}, \vec{K}) + e_j^*(\vec{P}, \vec{K}) \qquad (20)$$

and $(\epsilon_{ij}^*)_0$ is the starting energy. The single-particle energy e_i^* includes kinetic energy and potential energy contributions. The Pauli operator, Q_{ij}, prevents scattering to occupied nn, pp, or np states. To eliminate the angular dependence from the kernel of Eq. (17), it is customary to replace the exact Pauli operator with its angle-average. Detailed expressions for the Pauli operator and the average center-of-mass momentum in the case of two different Fermi seas can be found in (Alonso & Sammarruca, 2003).

With the definitions

$$G_{ij} = \frac{m_i^*}{E_i^*(\vec{q}')} g_{ij} \frac{m_j^*}{E_j^*(\vec{q})} \qquad (21)$$

and

$$V_{ij}^* = \frac{m_i^*}{E_i^*(\vec{q}')} v_{ij}^* \frac{m_j^*}{E_j^*(\vec{q})} , \qquad (22)$$

one can rewrite Eq. (17) as

$$G_{ij}(\vec{q}\,', \vec{q}, \vec{P}, (\epsilon_{ij}^*)_0) = V_{ij}^*(\vec{q}\,', \vec{q})$$

$$+ \int \frac{d^3 K}{(2\pi)^3} V_{ij}^*(\vec{q}\,', \vec{K}) \frac{Q_{ij}(\vec{K}, \vec{P})}{(\epsilon_{ij}^*)_0 - \epsilon_{ij}^*(\vec{P}, \vec{K})} G_{ij}(\vec{K}, \vec{q}, \vec{P}, (\epsilon_{ij}^*)_0) , \tag{23}$$

which is formally identical to its non-relativistic counterpart.

The goal is to determine self-consistently the nuclear matter single-particle potential which, in IANM, is different for neutrons and protons. To facilitate the description of the procedure, we will use a schematic notation for the neutron and proton potentials. We write, for neutrons,

$$U_n = U_{np} + U_{nn} , \tag{24}$$

and for protons

$$U_p = U_{pn} + U_{pp} , \tag{25}$$

where each of the four pieces on the right-hand-side of Eqs. (24-25) signifies an integral of the appropriate G-matrix elements (nn, pp, or np) obtained from Eq. (23). Clearly, the two equations above are coupled through the np component and so they must be solved simultaneously. Furthermore, the G-matrix equation and Eqs. (24-25) are coupled through the single-particle energy (which includes the single-particle potential, itself defined in terms of the G-matrix). So we have a coupled system to be solved self-consistently.

Before proceeding with the self-consistency, one needs an *ansatz* for the single-particle potential. The latter is suggested by the most general structure of the nucleon self-energy operator consistent with all symmetry requirements. That is:

$$\mathcal{U}_i(\vec{p}) = U_{S,i}(p) + \gamma_0 U_{V,i}^0(p) - \vec{\gamma} \cdot \vec{p}\, U_{V,i}(p) , \tag{26}$$

where $U_{S,i}$ and $U_{V,i}$ are an attractive scalar field and a repulsive vector field, respectively, with $U_{V,i}^0$ the timelike component of the vector field. These fields are in general density and momentum dependent. We take

$$\mathcal{U}_i(\vec{p}) \approx U_{S,i}(p) + \gamma_0 U_{V,i}^0(p) , \tag{27}$$

which amounts to assuming that the spacelike component of the vector field is much smaller than both $U_{S,i}$ and $U_{V,i}^0$. Furthermore, neglecting the momentum dependence of the scalar and vector fields and inserting Eq. (27) in the Dirac equation for neutrons or protons propagating in nuclear matter,

$$(\gamma_\mu p^\mu - m_i - \mathcal{U}_i(\vec{p})) u_i(\vec{p}, \lambda) = 0 , \tag{28}$$

naturally leads to rewriting the Dirac equation in the form

$$(\gamma_\mu (p^\mu)^* - m_i^*) u_i(\vec{p}, \lambda) = 0 , \tag{29}$$

with positive energy solutions as in Eq. (14), $m_i^* = m + U_{S,i}$, and

$$(p^0)^* = p^0 - U_{V,i}^0(p) . \tag{30}$$

The subscript "i" signifies that these parameters are different for protons and neutrons.

As in the symmetric matter case (Brockmann & Machleidt, 1990), evaluating the expectation value of Eq. (27) leads to a parametrization of the single particle potential for protons and neutrons [Eqs.(24-25)] in terms of the constants $U_{S,i}$ and $U_{V,i}^0$ which is given by

$$U_i(p) = \frac{m_i^*}{E_i^*} < \vec{p}|\mathcal{U}_i(\vec{p})|\vec{p} > = \frac{m_i^*}{E_i^*} U_{S,i} + U_{V,i}^0 . \tag{31}$$

Also,

$$U_i(p) = \sum_{j=n,p} \sum_{p' \leq k_F^j} G_{ij}(\vec{p}, \vec{p}') , \tag{32}$$

which, along with Eq. (31), allows the self-consistent determination of the single-particle potentials as explained below.

The kinetic contribution to the single-particle energy is

$$T_i(p) = \frac{m_i^*}{E_i^*} < \vec{p}|\vec{\gamma} \cdot \vec{p} + m|\vec{p} > = \frac{m_i m_i^* + \vec{p}^2}{E_i^*} , \tag{33}$$

and the single-particle energy is

$$e_i^*(p) = T_i(p) + U_i(p) = E_i^* + U_{V,i}^0 . \tag{34}$$

The constants m_i^* and

$$U_{0,i} = U_{S,i} + U_{V,i}^0 \tag{35}$$

are convenient to work with as they facilitate the connection with the usual non-relativistic framework (Haften & Tabakin, 1970).

Starting from some initial values of m_i^* and $U_{0,i}$, the G-matrix equation is solved and a first approximation for $U_i(p)$ is obtained by integrating the G-matrix over the appropriate Fermi sea, see Eq. (32). This solution is again parametrized in terms of a new set of constants, determined by fitting the parametrized U_i, Eq. (31), to its values calculated at two momenta, a procedure known as the "reference spectrum approximation". The iterative procedure is repeated until satisfactory convergence is reached.

Finally, the energy per neutron or proton in nuclear matter is calculated from the average values of the kinetic and potential energies as

$$\bar{e}_i = \frac{1}{A} < T_i > + \frac{1}{2A} < U_i > -m . \tag{36}$$

The EoS, or energy per nucleon as a function of density, is then written as

$$\bar{e}(\rho_n, \rho_p) = \frac{\rho_n \bar{e}_n + \rho_p \bar{e}_p}{\rho} , \tag{37}$$

or

$$\bar{e}(k_F, \alpha) = \frac{(1+\alpha)\bar{e}_n + (1-\alpha)\bar{e}_p}{2} . \tag{38}$$

Clearly, symmetric nuclear matter is obtained as a by-product of the calculation described above by setting α=0, whereas α=1 corresponds to pure neutron matter.

3.2.2 Microscopic predictions of the EoS and related quantities

In Fig. 3, we show EoS predictions for symmetric matter (solid red) and neutron matter (dashed black) as obtained from the Idaho calculation described in the previous section. The EoS from DBHF can be characterized as being moderately "soft" at low to medium density and fairly "stiff" at high densities. The predicted saturation density and energy for the symmetric matter EoS in Fig. 3 are equal to 0.185 fm^{-3} and -16.14 MeV, respectively, and the compression modulus is 252 MeV.

The increased stiffness featured by the DBHF EoS at the higher densities originates from the strongly density-dependent repulsion characteristic of the Dirac-Brueckner-Hartee-Fock method. In (Klähn et al., 2006), it is pointed out that constraints from neutron star phenomenology together with flow data from heavy-ion reactions suggest that such EoS behavior may be desirable.

The pressure as a function of density, as discussed in the next section, plays the crucial role in building the structure of a neutron star. In Fig. 4 we show the pressure in symmetric matter as predicted by the Idaho calculation compared with constraints obtained from flow data (Danielewicz et al., 2002). The predictions are seen to fall just on the high side of the constraints and grow rather steep at high density.

We show in Fig. 5 the pressure in neutron matter (red curve) and β-equilibrated matter (green) as predicted by DBHF calculations. The pressure contour is again from (Danielewicz et al., 2002).

Next we move on to the symmetry energy as defined from Eq. (6). In Fig. 6, we display the Idaho DBHF prediction for the symmetry energy by the solid red curve. The curve is seen to grow at a lesser rate with increasing density, an indication that, at large density, repulsion in the symmetric matter EoS increases more rapidly relative to the neutron matter EoS. This can be understood in terms of increased repulsion in isospin zero partial waves (absent from neutron matter) as a function of density. Our predicted value for the symmetry pressure L [see Eq. (8)], is close to 70 MeV.

The various black dashed curves in Fig. 6 are obtained with the simple parametrization

$$e_{sym} = C(\rho/\rho_0)^\gamma,$$ (39)

with γ increasing from 0.7 to 1.0 in steps of 0.1, and $C \approx 32$ MeV. Considering that all of the dashed curves are commonly used parametrizations suggested by heavy-ion data (Li & Chen, 2005), Fig. 6 clearly reflects our limited knowledge of the symmetry energy, particularly, but not exclusively, at the larger densities.

As already mentioned in Section **2**, from the experimental side intense effort is going on to obtain reliable empirical information on the less known aspects of the EoS. Heavy-ion reactions are a popular way to seek constraints on the symmetry energy, through analyses of observables that are sensitive to the pressure gradient between nuclear and neutron matter.
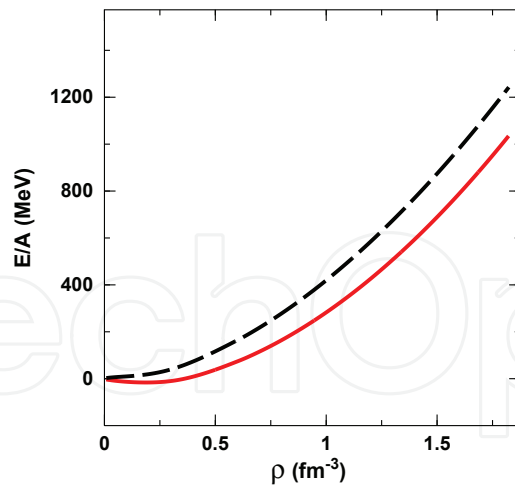
Fig. 3. DBHF predictions for the EoS of symmetric matter (solid red) and neutron matter (dashed black).
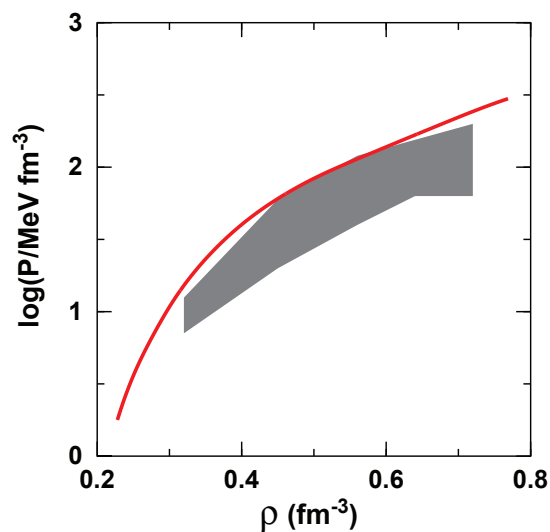

Fig. 4. Pressure in symmetric matter from the Idaho DBHF calculation. The shaded area corresponds to the region of pressure consistent with the flow data analysed in (Danielewicz et al., 2002).

We close this Section with demonstrating the approximately linear dependence on the asymmetry parameter of the single-nucleon potentials in IANM as anticipated in Eq. (10). We recall that this isospin splitting is the crucial mechanism that separates proton and neutron dynamics in IANM. In Fig. 7 we display predictions obtained with three different NN potentials based on the one-boson-exchange model, Bonn A, B, and C (Machleidt, 1989). These three models differ mainly in the strength of the tensor force, which is mostly carried by partial waves with isospin equal to 0 (absent from pure neutron matter) and thus should fade away in the single-neutron potential as the neutron fraction increases. In fact, the figure demonstrates reduced differences among the values of U_n predicted with the three potentials at large α.
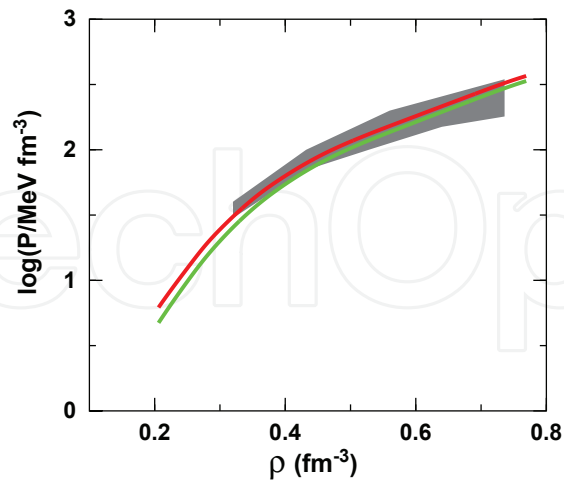
Fig. 5. Pressure in neutron (red curve) and baryon-lepton (green curve) matter from the Idaho DBHF calculation. The shaded area corresponds to the region of pressure consistent with flow data and the inclusion of strong density dependence in the asymmetry term (Danielewicz et al., 2002).
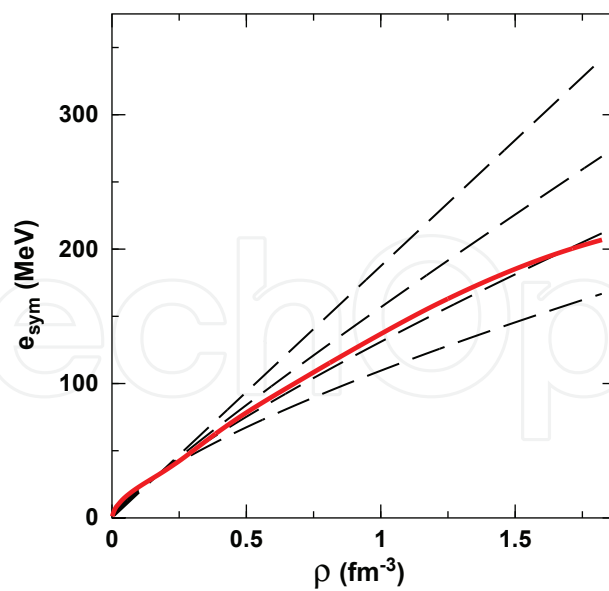

Fig. 6. DBHF prediction for the symmetry energy (solid red) compared with various phenomenological parametrizations (dashed black), as explained in the text.
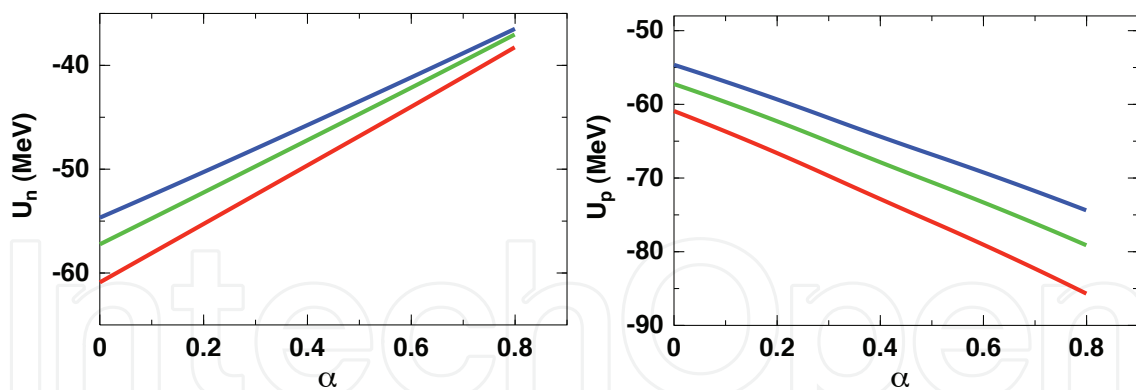
Fig. 7. The neutron and proton single-particle potentials as a function of the asymmetry parameter at fixed average density and momentum equal to the average Fermi momentum, which is chosen to be 1.4 fm^{-1}. The red, green, and blue lines represent the predictions from the Bonn A, B, and C potentials, respectively.

4. Neutron stars

4.1 A brief review of basic structure equations and available constraints

Fusion reactions in stars give rise to elements, but at the same time exhaust the nuclear fuel. After the fuel is exhausted, the star can die through four possible channels: it can become a black hole, a white dwarf, a neutron star, or it can disassemble completely. The ultimate outcome depends on the mass of the original star. If the mass is larger than about four solar masses, the star may become a supernova which, in turn, may result either in a neutron star or a black hole.

Neutron stars contain the most dense form of matter found in the universe and, therefore, are unique laboratories to study the properties of highly compressed (cold) matter. They are held together by gravity and neutron degeneracy pressure. (In contrast, white dwarfs are kept in hydrostatic equilibrium by gravity and electron degeneracy pressure.)

Although neutron stars were predicted as early as in the 1930's, hope for their observation remained slim for a long time. In 1967, strange new objects, outside the solar system, were observed at the University of Cambridge. They were named *pulsars*, as they emitted periodic radio signals. To date, about 1700 pulsars have been detected, many in binary systems.

Typically, detection of thermal radiation from the surface of a star is the way to access information about its properties. Furthermore, the possibility of exploring the structure of neutron stars via gravitational waves makes these exotic objects even more interesting.

The densities found in neutron stars range from the density of iron to several times normal nuclear density. Most of the mass consists of highly compressed matter at nuclear and supernuclear densities. The *surface* region is composed of normal nuclei and non-relativistic electrons, with typical mass densities in the range 10^4 g cm$^{-3} \leq \epsilon \leq 10^6$ g cm^{-3}. As density increases, charge neutrality requires matter to become more neutron rich. In this density range (about 10^6 g cm$^{-3} < \epsilon < 10^{11}$ g cm^{-3}), neutron-rich nuclei appear, mostly light metals, while electrons become relativistic. This is the *outer crust*. Above densities of approximately 10^{11} g cm^{-3}, free neutrons begin to form a continuum of states. The *inner crust* is a compressed solid with a fluid of neutrons which drip out and populate free states outside the nuclei, since

those have become neutron-saturated. Densities in the inner crust range between 10^{11} g cm^{-3} and 10^{14} g cm^{-3}. At densities equal to approximately 1/2 of saturation density, clusters begin to merge into a continuum. In this phase, matter is a uniform fluid of neutrons, protons, and leptons. Above a few times nuclear matter density, the actual composition of stellar matter is not known. Strange baryons can appear when the nucleon chemical potential is of the order of their rest mass. Meson production can also take place. At even higher densities, transitions to other phases are speculated, such as a deconfined, rather than hadronic, phase. The critical density for such transition cannot be predicted reliably because it lies in a range where QCD is non perturbative (Sedrakian, 2007).

The possibility has been speculated that the most stable state at zero pressure may be u, d, s quark matter instead of iron. This would imply that strange quark matter is the most stable (in fact, the absolutely stable) state of strongly interacting matter, as originally proposed by Bodmer (Bodmer, 1971), Witten (Witten, 1984), and Terazawa (Terazawa, 1989). In such case, hyperonic and hybrid stars would have to be metastable with respect to stars composed of stable three-flavor strange quark matter (Weber, 1999), which is lower in energy than two-flavor quark matter due to the extra Fermi levels open to strange quarks. Whether or not strange quark stars can give rise to pulsar glitches (which are observed sudden small changes in the rotational frequency of a pulsar), may be a decisive test of the strange quark matter hypothesis (Weber, 1999).

The maximum gravitational mass of the star and the corresponding radius are the typical observables used to constraint the EoS. The gravitational mass is inferred mostly from observations of X-ray binaries or binary pulsars. Determination of the mass provide a unique test of both theories of nuclear matter and general relativity. The pulsar in the Hulse-Taylor binary system has a mass of 1.4408 ± 0.0003 $M_\odot$, to date the best mass determination.

At this time, one of the heaviest neutron stars (with accurately known mass) has a mass of 1.671 ± 0.008 $M_\odot$ (Champion et al., 2008). The observation of an even heavier star has been confirmed recently, namely J1614-2230, with a mass of 1.97 ± 0.04 $M_\odot$ (Demorest et al., 2010). This value is the highest measured with this certainty and represents a challenge for the softest EoS. We also recall that an initial observation of a neutron star in a binary system with a white dwarf had suggested a neutron star mass (PSR J0751+1807) of $2.1 \pm 0.2 M_\odot$ (Nice et al., 2005). Such observation, which would imply a considerable constraint on the high-density behavior of the EoS, was not confirmed.

The minumum mass of a neutron star is also a parameter of interest. For a cold, stable system, the minimum mass is estimated to be 0.09 $M_\odot$ (Lattimer & Prakash, 2007). The smallest reliably estimated neutron star mass is the companion of the binary pulsar J1756-2251, which has a mass of 1.18 ± 0.02 $M_\odot$ (Faulkner et al., 2004).

Measurements of the radius are considerably less precise than mass measurements (Lattimer & Prakash, 2007). No direct measurements of the radius exist. Instead, the observed X-ray flux, together with theoretical assumptions (Weber, 1999), can provide information on the radiation or photospheric radius, R_∞, which is related to the actual stellar radius by $R_\infty = R(1 - 2GM/Rc^2)^{-1/2}$. Estimates are usually based on thermal emission of cooling stars, including redshifts, and the properties of sources with bursts or thermonuclear explosions at the surface. A major problem associated with the determination of radii is that the distance from the source is not well known, hence the need for additional assumptions. Much more

stringent constraints could be imposed on the EoS if mass and radius were determined independently from each other.

Another bulk property of neutron stars is the moment of inertia, I. For softer EoS, both mass and radius are smaller and so is I. From observations of the Crab nebula luminosity, a lower bound on the moment of inertia was inferred to be $I \geq$ 4-8 $\times 10^{44}$ g cm^2, see (Weber, 1999) and references therein. A measurement of the moment of inertia within 10%, together with the information on the mass, would be able to discriminate among various EoS (Lattimer & Prakash, 2007). To date, the best determination of the moment of inertia is the one for the Crab pulsar (Beiger & Haensel, 2003) which would rule out only very soft EoS (Lattimer & Prakash, 2007).

A proton-neutron star is the result of a supernova explosion resulting from the gravitational collapse of a massive star core. Nearly all of the remaining binding energy is carried away by neutrinos during the first few tens of seconds of the evolution. Thus neutrino emission is very efficient as a cooling mechanism, with the internal temperature dropping to about 10^{10} K within a few days. Cooling through neutrino emission continues for a long time (in the order of 1,000 years), until the temperature drops to about 10^8 K, at which point photon emission becomes the dominant cooling mechanism. Neutrino luminosity and emission timescale are controlled by several factors including the total mass of the (proton-neutron) star and the opacity of neutrinos at high densities, which is sensitive to the EoS of dense hadronic matter.

Gravitational waves are a less conventional way to probe neutron star properties. Compact stars in binary systems are epected to produce gravitational radiation. In turn, emission of gravitational waves causes decay of the mutual orbits and eventually merger of the binary system. Because of the merger timescale (250 million years for PSR B1913+16, for instance, and 85 million years for PSR J0737-3039), it can be expected that many such decaying binary systems exist in the galaxy and emit large amounts of gravitational radiation. The observation of gravitational waves has the potential to set strong constraints on masses and radii, see see (Lattimer & Prakash, 2007) and references therein.

A theoretical estimate of the maximum possible mass of a neutron star was performed by Rhoades and Ruffini (Rhoades & Ruffini, 1974) on the following assumptions: 1) General relativity is the correct theory of gravitation; 2) the EoS satisfy the Le Chatelier's principle ($\partial P / \partial \epsilon \geq 0$) and the causality condition, $\partial P / \partial \epsilon \leq c^2$; and 3) the EoS below some matching density is known. On this basis, they determined that the maximum mass of a neutron star cannot exceed 3.2 solar masses. Abandoning the causality condition, which would hold exactly only if stellar matter is neither dispersive nor absorptive, this limit can be as high as 5 solar masses due to the increased stiffness of the EoS at supernuclear densities.

The maximum mass and the radius of a neutron star are sensitive to different aspects of the EoS. The maximum mass is mostly determined by the stiffness of the EoS at densities greater than a few times saturation density. The star radius is mainly sensitive to the slope of the symmetry energy. In particular, it is closely connected to the internal pressure (that is, the energy gradient) of matter at densities between about $1.5\rho_0$ and 2-3ρ_0 (Lattimer & Prakash, 2007). Non-nucleonic degrees of freedom, which typically make their appearance at those densities, are known to have a considerable impact on the maximum mass of the star. The latter is predicted by the equation of hydrostatic equilibrium for a perfect fluid.

In general relativity, the invariant interval between two infinitesimally close space-time events is given by

$$ds^2 = g_{\alpha\beta}dx^\alpha dx^\beta \, , \tag{40}$$

where $g_{\alpha\beta}$ is the space-time metric. For a spherically symmetric space-time, the most general static line element consistent with all required symmetries has the form

$$ds^2 = -f(r)dt^2 + g(r)dr^2 + h^2(r)(sin^2\theta \, d\phi^2 + d\theta^2) \, . \tag{41}$$

Choosing a radial coordinate r such that $h^2(r) = r^2$ yields the so-called "standard" form of the metric.

The equation of hydrostatic equilibrium (the TOV equation) determines the form of the metric functions along with the pressure and the total mass-energy density as a function of the radial coordinate in the interior of the star. It reads

$$\frac{dP(r)}{dr} = -\frac{G}{c^2}\frac{(P(r) + \epsilon(r))(M(r) + 4\pi r^3 P(r)/c^2)}{r(r - 2GM(r)/c^2)} \, , \tag{42}$$

with

$$\frac{dM(r)}{dr} = 4\pi r^2\epsilon(r) \, , \tag{43}$$

where ϵ is the total mass-energy density. The star *gravitational* mass is

$$M(R) = \int_0^R 4\pi r^2\epsilon(r)dr \, , \tag{44}$$

where R is the value of r where the pressure vanishes. It's worth recalling that no mass limit exists in Newtonian gravitation.

The pressure is related to the energy per particle through

$$P(\rho) = \rho^2\frac{\partial e(\rho)}{\partial\rho} \, . \tag{45}$$

The structure equations of rotationally deformed compact stars are much more complex than those of spherically symmetric stars (Weber, 1999) presented here. The most rapidly rotating pulsar, PSR J1748-2446 (Hessels et al., 2006), is believed to rotate at a rate of 716 Hz, although an X-ray burst oscillation at a frequency of 1122 Hz was reported (Kaaret et al., 2006), which may be due to the spin rate of a neutron star. Naturally, the maximum mass and the (equatorial) radius become larger with increasing rotational frequency.

4.2 Composition of β-stable matter

Assuming that only neutrons, protons, and leptons are present, the proton fraction in stellar matter under conditions of β-equilibrium is calculated by imposing energy conservation and charge neutrality. The resulting algebraic equations can be found in standard literature (Glendenning, 1997). The contribution to the energy density from the electrons is written as

$$e_e = \frac{\hbar c}{4\pi^2}(3\pi^2\rho_e)^{4/3} \, , \tag{46}$$

whereas for muons we write

$$e_\mu = \rho_\mu m_\mu c^2 + (\hbar c)^2 \frac{(3\pi^2 \rho_\mu)^{5/3}}{10\pi^2 m_\mu c^2} . \qquad (47)$$

These contributions are added to the baryonic part to give the total energy density. The derivative of the total energy per particle with respect to the fraction of a particular species is the chemical potential of that species. The conditions

$$\mu_p + \mu_e = \mu_n \; ; \; \mu_\mu = \mu_e \; ; \; \rho_p = \rho_\mu + \rho_e \, , \qquad (48)$$

allow to solve for the densities (or fractions) of protons, electrons, and muons. Near the saturation density, when the muon fraction is close to zero, one can estimate the equilibrium proton fraction, x_p, to be (Lattimer & Prakash, 2007)

$$x_p \approx \left(\frac{4e_{sym}(\rho_0)}{\hbar c} \right)^3 / (3\pi^2 \rho_0). \qquad (49)$$

The fractions of protons, electrons, and muons as predicted with the DBHF equation of state are shown in Fig. 8. The critical density for the proton fraction to exceed approximately 1/9 and, thus, allow cooling through the direct Urca processes,

$$n \to p + e + \bar{\nu}_e \quad and \quad p + e \to n + \nu_e \, , \qquad (50)$$

is about $0.36 - 0.39$ fm^{-3}. Notice that, due to the relation between symmetry energy and proton fraction, large values of the symmetry energy would make the star cool rapidly. In fact, already in earlier studies (Boguta, 1981) tha rapid cooling of neutron stars and the corresponding high neutrino luminosity was understood in terms of neutron β decay and large proton fractions.

At densities close to normal nuclear density, protons and neutrons are the only baryonic degrees of freedom. As density increases, other baryons begin to appear, such as strange baryons or isospin 3/2 nucleon resonances. Hyperonic states can be classified according to the irreducible representation of the $SU(3)$ group. The octet of baryons that can appear in neutron matter includes nucleons, Λ, $\Sigma^{0,\pm}$, and $\Xi^{0,-}$.

Neglecting the nucleon-hyperon interaction, the threshold for stable hyperons to exist in matter is determined by comparing the hyperon mass with the neutron Fermi energy, which is the largest available energy scale in neutron-rich matter. We consider cold neutron stars, after neutrinos have escaped. Strange baryons appear at about 2-3 times normal density (Baldo et al., 1998), an estimate which is essentially model independent, through the processes $n + n \to p + \Sigma^-$ and $n + n \to n + \Lambda$. The equilibrium conditions for these reactions are

$$2\mu_n = \mu_p + \mu_{\Sigma^-} \; ; \; \mu_n = \mu_\Lambda . \qquad (51)$$

Also, we have

$$\mu_e = \mu_\mu \; ; \; \mu_n = \mu_p + \mu_e \, , \qquad (52)$$

the equations above being special cases of

$$\mu = b\mu_n - q\mu_e, \tag{53}$$

where b and q are the baryon number and the charge (in units of the electron charge) of the particular species with chemical potential μ. Together with the charge neutrality condition and baryon number conservation,

$$\rho_p = \rho_e + \rho_\mu + \rho_{\Sigma^-} \; ; \; \rho = \rho_n + \rho_p + \rho_{\Sigma^-} + \rho_\Lambda, \tag{54}$$

the above system allows to determine the various particle fractions.

Naturally, the composition of matter at supra-nuclear densities determines the behavior of stellar matter. It is also speculated that a transition to a quark phase may take place at very high densities, the occurrence of which depends sensitively on the properties of the EoS in the hadronic (confined) phase. The presence of hyperons in the interior of neutron stars is reported to soften the equation of state, with the consequence that the predicted neutron star maximum masses become considerably smaller (Schulze et al., 2006). Strange baryons are not included in the predictions shown below.
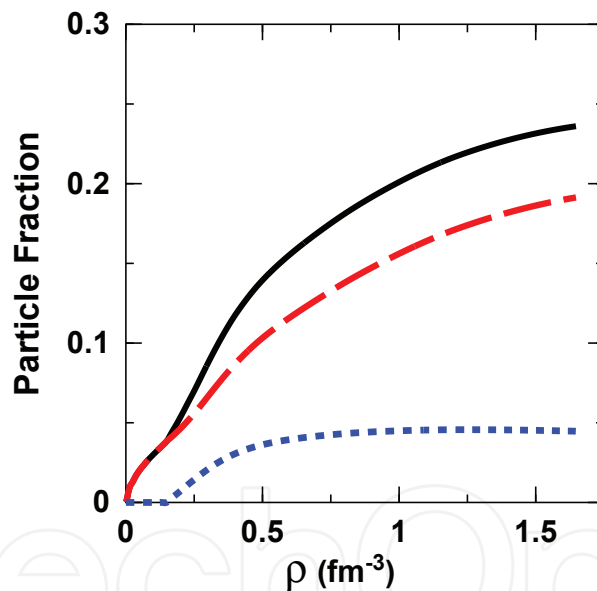
Fig. 8. Proton (solid black), electron (dashed red), and muon (dotted blue) fractions in β-stable matter as a function of total baryon density as predicted by the DBHF model.

4.3 Microscopic predictions of neutron star properties

We are now ready to move to applications of our EoS to compact stars.

As explained in Section **3**, the DBHF model does not include three-body forces explicitly, but effectively incorporates the class of TBF originating from the presence of nucleons and antinucleons (the "Z-diagrams" in Fig. 2), see discussion in Section **3.1**. In order to broaden our scopes, we will compare our predictions with those of other microscopic models. As the other element of our comparison, we will take the EoS from the microscopic approach of (Li
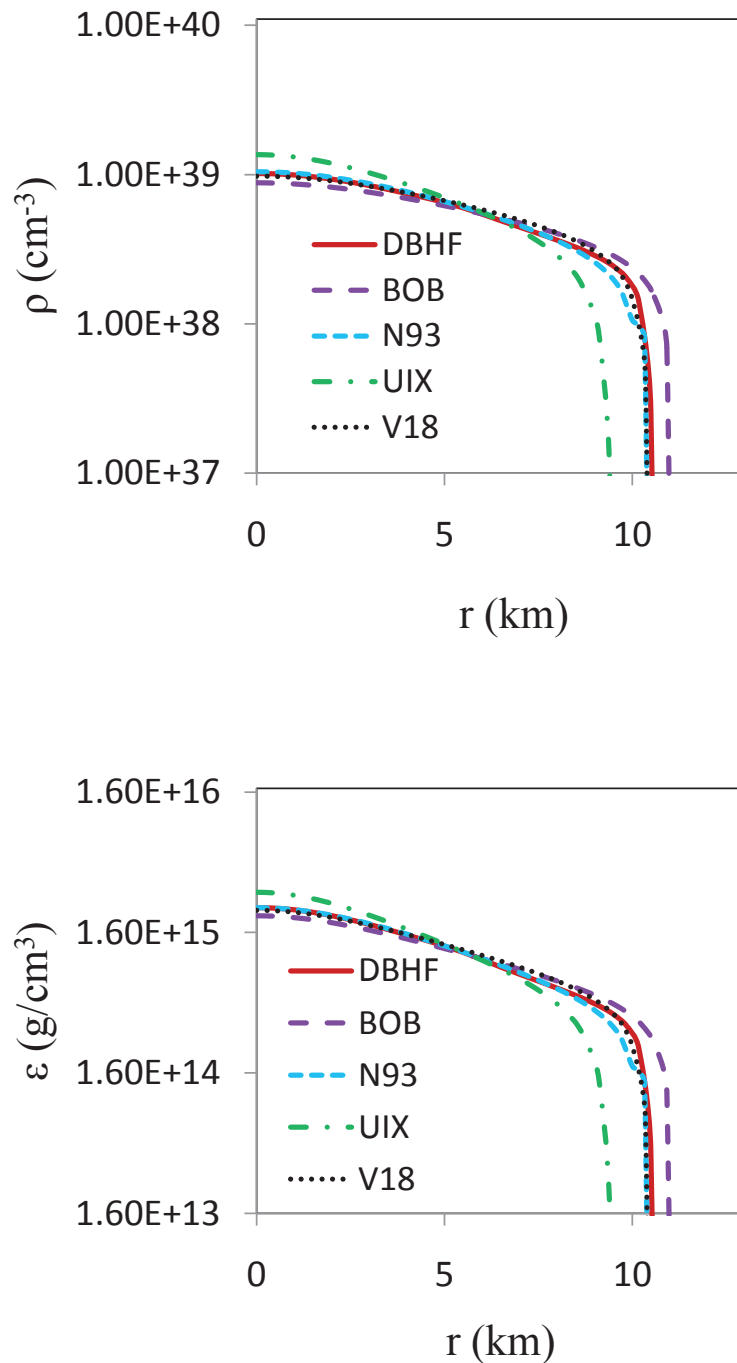
Fig. 9. The baryon density and the mass-energy density profile for a neutron star with the maximum mass allowed by each EoS model.

et al., 2008). There (and in previous work by the same authors), the Brueckner-Hartree-Fock (BHF) formalism is employed along with microscopic three-body forces. In particular, in (Li & Schulze, 2008) the meson-exchange TBF are constructed applying the same parameters as used in the corresponding nucleon-nucleon potentials, which are: Argonne V18 (Wiringa et al., 1995) (V18), Bonn B (Machleidt, 1989) (BOB), Nijmegen 93 (Stocks et al., 1994) (N93). The popular (but phenomenological) Urbana TBF (Pieper et al., 2001) (UIX) is also utilized in (Li &
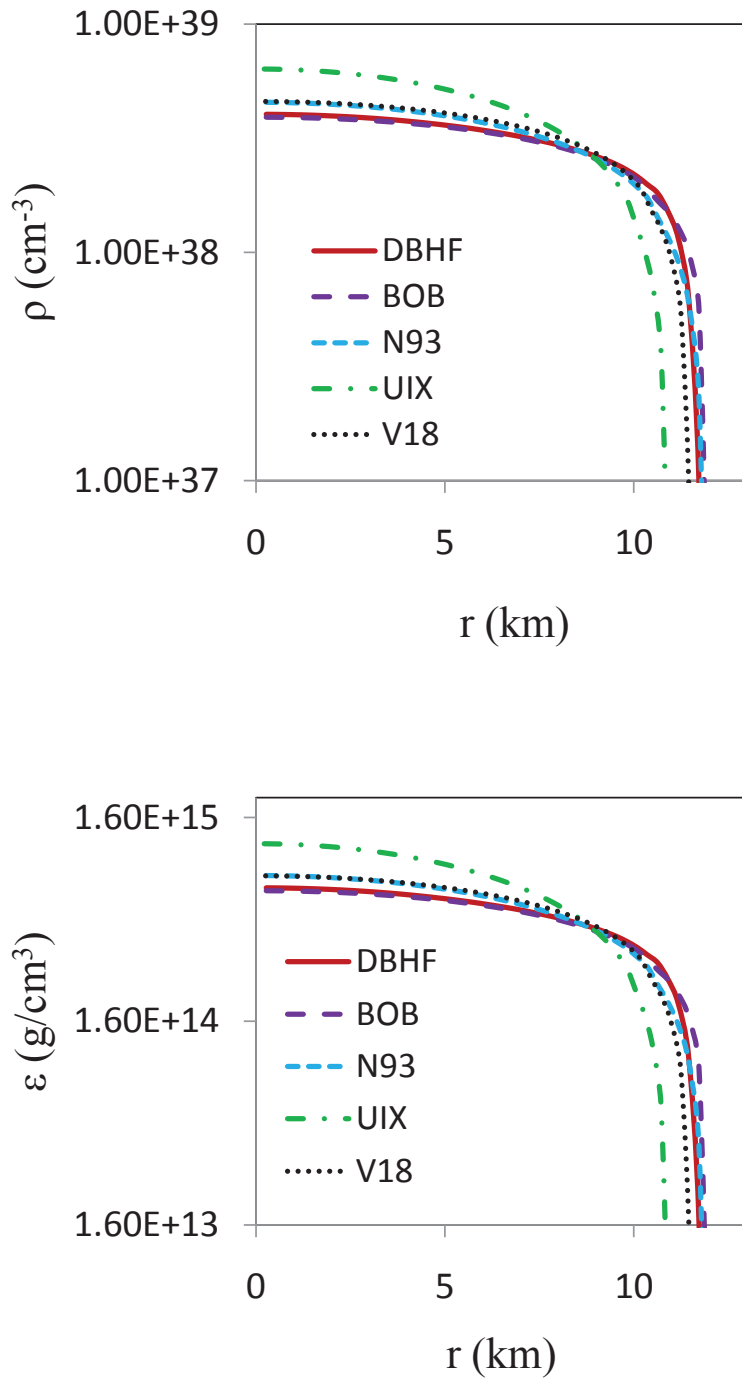
Fig. 10. The baryon density and the mass-energy density profile for a neutron star with a mass of 1.4 solar masses.

Schulze, 2008). Convenient parametrizations in terms of simple analytic functions are given in all cases and we will use those to generate the various EoS. We will refer to this approach, generally, as "BHF + TBF".

At subnuclear densities all the EoS considered here are joined with the crustal equations of state from Harrison and Wheeler (Harrison et al., 1965) and Negele and Vautherin (Negele &
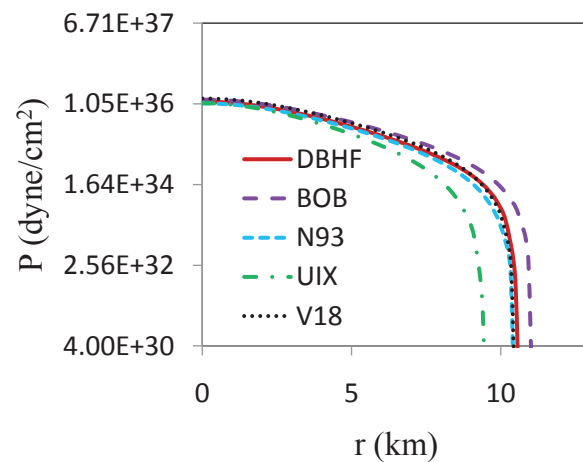
Fig. 11. Pressure profile for the maximum-mass star allowed by each EoS model.
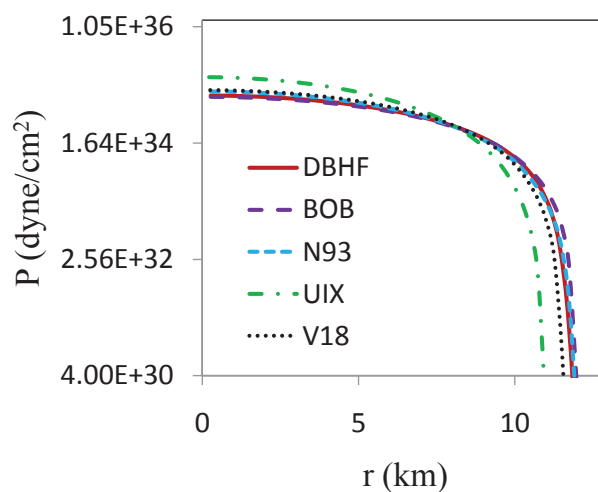
Fig. 12. Pressure profile predicted by the various models for a 1.4 solar mass star.

Vautherin, 1973). The composition of the crust is crystalline, with light (Harrison et al., 1965) or heavy (Negele & Vautherin, 1973) metals and electron gas.

We begin with showing the baryon number density and the mass-energy density profile of the star, see Fig. 9. For each EoS model, the maximum mass configuration is considered. Thus the models differ in their central density, which, in turn, impact the radius. The relations shown in Fig. 9 are insightful, as they reveal the detailed structure of the star at each radial position. Furthermore, the compactness of the star, whose density profile is reminescent of the one in a nucleus, a system 55 orders of magnitude lighter, is apparent. In Fig. 10, the same quantities are shown for a star with a mass of 1.4 solar masses, the most probable mass of a neutron star.

The models labeled as UIX and BOB have the smallest and largest radius, respectively, as can be seen from the figure. We also see that the star's outer regions, that is, for energy densities less than about 10^{14} g cm^{-3}, are influenced quite strongly by differences in the various EoS models. Note that the UIX model, with the smallest radius, can tolerate larger central densities.
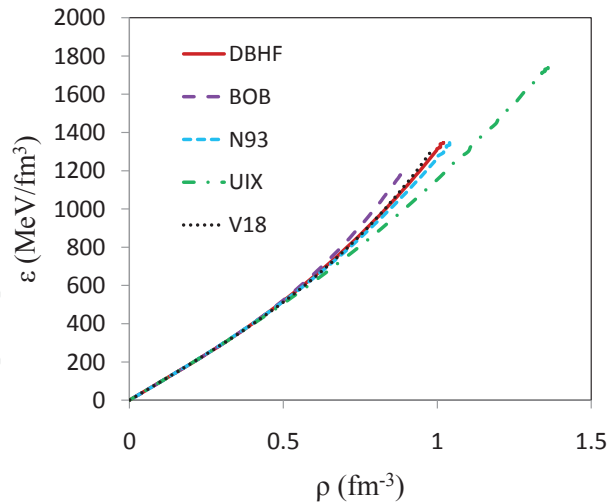
Fig. 13. Energy density *vs.* baryon number density for the various EoS being addressed in the text. The maximum-mass model is considered in each case.

Of interest is also the pressure profile for the maximum-mass star in each model, which is shown in Fig. 11 for the maximum mass and in Fig. 12 for a 1.4 solar mass star.

The $\epsilon(r)$ and $\rho(r)$ relations from Fig. 9 are combined to provide the $\epsilon(\rho)$ relation within the star as shown in Fig. 13 for the maximum mass. Again, we see that the stiffest (BOB) and softest EoS (UIX) support the smallest and largest central densities, respectively. At the same time, these two EoS predict the largest (BOB) and smallest (UIX) maximum mass, see below.

In Fig. 14, we show the mass-radius relation for a sequence of static neutron stars as predicted by the various models. All models besides DBHF share the same many-body approach (BHF+TBF) but differ in the two-body potential and TBF employed. The differences resulting from the use of different NN potentials can be larger than those originating from emplying different many-body approaches. This can be seen by comparing the DBHF and BOB curves, both employing the Bonn B interaction (although in the latter case the non-relativistic, r-space version of the potential is adopted). Overall, the maximum masses range from $1.8 M_\odot$ (UIX) to $2.5 M_\odot$ (BOB). Radii are less sensitive to the EoS and range between 10 and 12 km for all models under consideration, DBHF or BHF+TBF. Concerning consistency with present constraints, the observations reported in Section **4.1** would appear to invalidate only the model with the smallest maximum mass, UIX. Notice, further, that phenomena such as condensation of mesons may soften the EoS considerably at supernuclear density as condensation would bring loss of pressure.

Also of interest is the star baryon number, A, which is obtained by integrating the baryon density over the proper volume (Weber, 1999). Namely,

$$A = 4\pi \int_0^R dr\, r^2 \frac{\rho(r)}{\sqrt{1 - 2GM(r)/(rc^2)}} \; . \tag{55}$$

Defining the star's baryon mass as

$$M_A = m_n A \; , \tag{56}$$

where m_n is the mass of the baryon, one can calculates the star's binding energy, defined as

$$E_B = M - M_A \ .\tag{57}$$

The baryon number and the star binding energy as a function of the central density (in units of nuclear matter density) are shown in Fig. 15 and Fig. 16 for the various models. We see that the baryon number for stable stars is approximately equal to $10^{56} - 10^{57}$. A much higher value would make the star unstable with respect to gravitational collapse. The binding energy displayed in Fig. 16 is defined in units of the solar mass. Typically, the binding energy changes the sign for masses less than 0.1 solar masses. The binding energy is a potentially observable quantity, since neutrinos from a supernova carry information about the gravitational binding energy of the neutron star that has resulted from the explosion.

Next, we calculate the gravitational redshift predicted by each model. The redshift is defined as

$$z = \frac{\nu_E}{\nu_\infty} - 1 \ ,\tag{58}$$

where ν_E and ν_∞ are the photon frequencies at the emitter and at the infinitely far receiver. The photon frequency at the emitter is the inverse of the proper time between two wave crests in the frame of the emitter,

$$\frac{1}{d\tau_E} = (-g_{\mu\nu}dx^\mu dx^\nu)_E^{-1/2} \ ,\tag{59}$$

with a similar expression for the frequency at the receiver. Then

$$\frac{\nu_\infty}{\nu_E} = \frac{((-g_{00})^{1/2}dx^0)_E}{((-g_{00})^{1/2}dx^0)_\infty} \ .\tag{60}$$

Assuming a static gravitational field, in which case the time dx^0 between two crests is the same at the star's surface and at the receiver, and writing g_{00} as the metric tensor component at the surface of a nonrotating star yield the simple equation

$$z = \left(1 - \frac{2MG}{Rc^2}\right)^{-1/2} - 1 \ .\tag{61}$$

Notice that simultaneous measurements of R_∞ and z determines both R and M, since

$$R = R_\infty(1+z)^{-1} \ ,\tag{62}$$

and

$$M = \frac{c^2}{2G}R_\infty(1+z)^{-1}[1 - (1+z)^{-2}] \ .\tag{63}$$

In Fig. 17 we show the gravitational redshift as a function the mass for each model. Naturally the rotation of the star modifies the metric, and in that case different considerations need to be applied which result in a frequency dependence of the redshift. We will not consider the general case here.

We conclude this section with showing a few predictions for the case of rapidly rotating stars. The model dependence of the mass-radius relation is shown in Fig. 18. The 716 Hz frequency corresponds to the most rapidly rotating pulsar, PSR J1748-2446, (Hessels et al., 2006) although
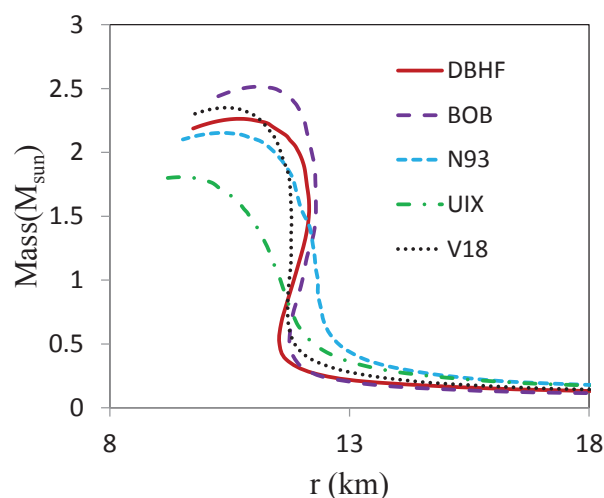
Fig. 14. Static neutron star mass-radius relation for the models considered in the text.

recently an X-ray burst oscillation at a frequency of 1122 Hz has been reported (Kaaret et al., 2006) which may be due to the spin rate of a neutron star. As expected, the maximum mass and the (equatorial) radius become larger with increasing rotational frequency.

In Fig. 19, we show the moment of inertia at different rotational speeds (again, for all models). These values are not in contradiction with observations of the Crab nebula luminosity, from which a lower bound on the moment of inertia was inferred to be $I \geq$ 4-8 $\times 10^{44}$ g cm^2, see (Weber, 1999) and references therein.

Clearly, at the densities probed by neutron stars the model dependence is large, but presently available constraints are still insufficient to discriminate among these EoS. The model dependence we observe comes from two sources, the two-body potential and the many-body approach, specifically the presence of explicit TBF or Dirac effects. The dependence on the two-body potential is very large. Typically, the main source of model dependence among NN potentials is found in the strength of the tensor force. Of course, differences at the two-body level impact the TBF as well, whether they are microscopic or phenomenological.

5. Polarized isospin-asymmetric matter

Before concluding this chapter, we like to touch upon the issue of polarization in IANM.

When both isospin and spin asymmetries are present, constraints are much more difficult to obtain and predictions regarding magnetic properties of nuclear matter are sometimes found to be in qualitative disagreement with one another. This is especially the case with regard to the possibility of spontaneous phase transitions into spin ordered states, ferromagnetic (FM, with neutron and proton spins alligned), or antiferromagnetic state (AFM, with opposite spins for neutrons and protons). Notice that the presence of polarization would impact neutrino cross section and luminosity, resulting into a very different scenario for neutron star cooling, which is why we find it appropriate to briefly discuss this issue here.

Recently, we have extended the framework described in Section **3** (Sammarruca, 2011) to include both spin and isospin asymmetries of nuclear matter and calculated the energy per particle under extreme conditions of polarization. The existence (or not) of a possible phase
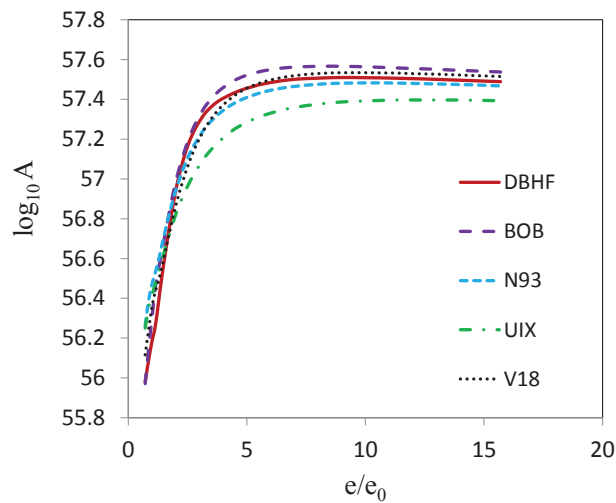
Fig. 15. Baryon number as a function of the central density (in units of $e_0 = 2.5 \, 10^{14} \, \mathrm{g \, cm^{-3}}$) for the models considered in the text.
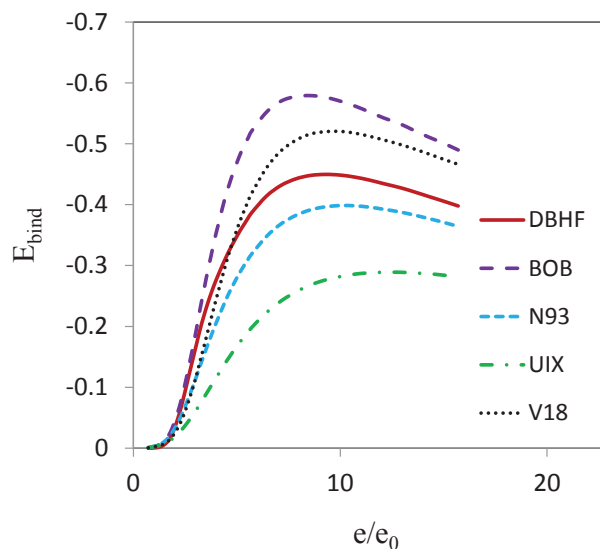

Fig. 16. Binding energy (in units of the solar mass) as a function of the central density for the EoS models considered in the text.

transition can be argued by comparing the energies of the fully polarized and the unpolarized phases.

In a spin-polarized and isospin asymmetric system with fixed total density, ρ, the partial densities of each species are

$$\rho_n = \rho_{nu} + \rho_{nd} \, , \quad \rho_p = \rho_{pu} + \rho_{pd} \, , \quad \rho = \rho_n + \rho_p \, , \tag{64}$$

where u and d refer to up and down spin-polarizations, respectively, of protons (p) or neutrons (n). The isospin and spin asymmetries, α, β_n, and β_p, are defined in a natural way:

$$\alpha = \frac{\rho_n - \rho_p}{\rho} \, , \quad \beta_n = \frac{\rho_{nu} - \rho_{nd}}{\rho_n} \, , \quad \beta_p = \frac{\rho_{pu} - \rho_{pd}}{\rho_p} \, . \tag{65}$$
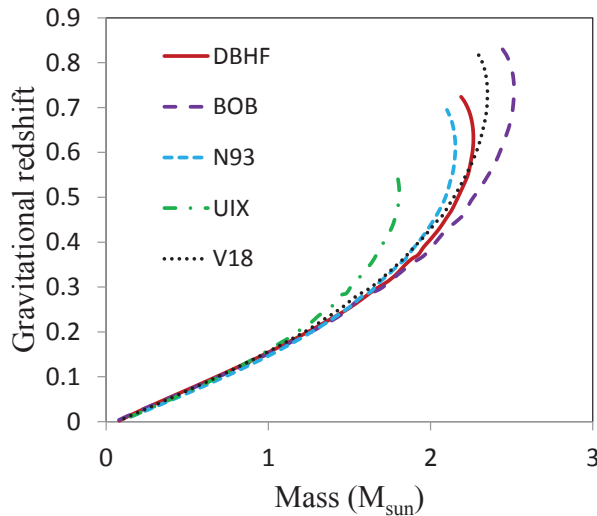
Fig. 17. Gravitational redshift for all models. For each model, the corresponding sequence of static stars is considered.

The single-particle potential of a nucleon in a particular $\tau\sigma$ state, $U_{\tau\sigma}$, is now the solution of a set of four coupled equations, which are the appropriate extension of Eqs. (24-25). They read

$$U_{nu} = U_{nu,nu} + U_{nu,nd} + U_{nu,pu} + U_{nu,pd} \tag{66}$$

$$U_{nd} = U_{nd,nu} + U_{nd,nd} + U_{nd,pu} + U_{nd,pd} \tag{67}$$

$$U_{pu} = U_{pu,nu} + U_{pu,nd} + U_{pu,pu} + U_{pu,pd} \tag{68}$$

$$U_{pd} = U_{pd,nu} + U_{pd,nd} + U_{pd,pu} + U_{pd,pd}\,, \tag{69}$$

to be solved self-consistently along with the two-nucleon G-matrix. In the above equations, each $U_{\tau\sigma,\tau'\sigma'}$ term contains the appropriate (spin and isospin dependent) part of the interaction, $G_{\tau\sigma,'\tau'\sigma'}$. More specifically,

$$U_{\tau\sigma}(\vec{k}) = \sum_{\sigma'=u,d} \sum_{\tau'=n,p} \sum_{q\leq k_F^{\tau'\sigma'}} < \tau\sigma, \tau'\sigma'|G(\vec{k},\vec{q})|\tau\sigma, \tau'\sigma' >, \tag{70}$$

where the third summation indicates integration over the Fermi seas of protons and neutrons with spin-up and spin-down. Notice that this equation is the extension of Eq. (32) in the presence of spin polarization.

In the left panel of Fig. 20, we show, in comparison with unpolarized symmetric matter (solid line): the EoS for the case of fully polarized neutrons and completely unpolarized protons (dashed line); the EoS for the case of protons and neutrons totally polarized in the same direction, that is, matter in the ferromagnetic (FM) state (dashed-dotted line); the EoS for the case of protons and neutrons totally polarized in opposite directions, namely matter in the antiferromagnetic (AFM) state (dotted line). A similar comparison is shown in the right panel of Fig. 20, but for isospin asymmetric matter. (Notice that all predictions are invariant under a global spin flip.)

We conclude that, for both symmetric and asymmetric matter, the energies of the FM and AFM states are higher than those of the corresponding unpolarized cases, with the AFM state
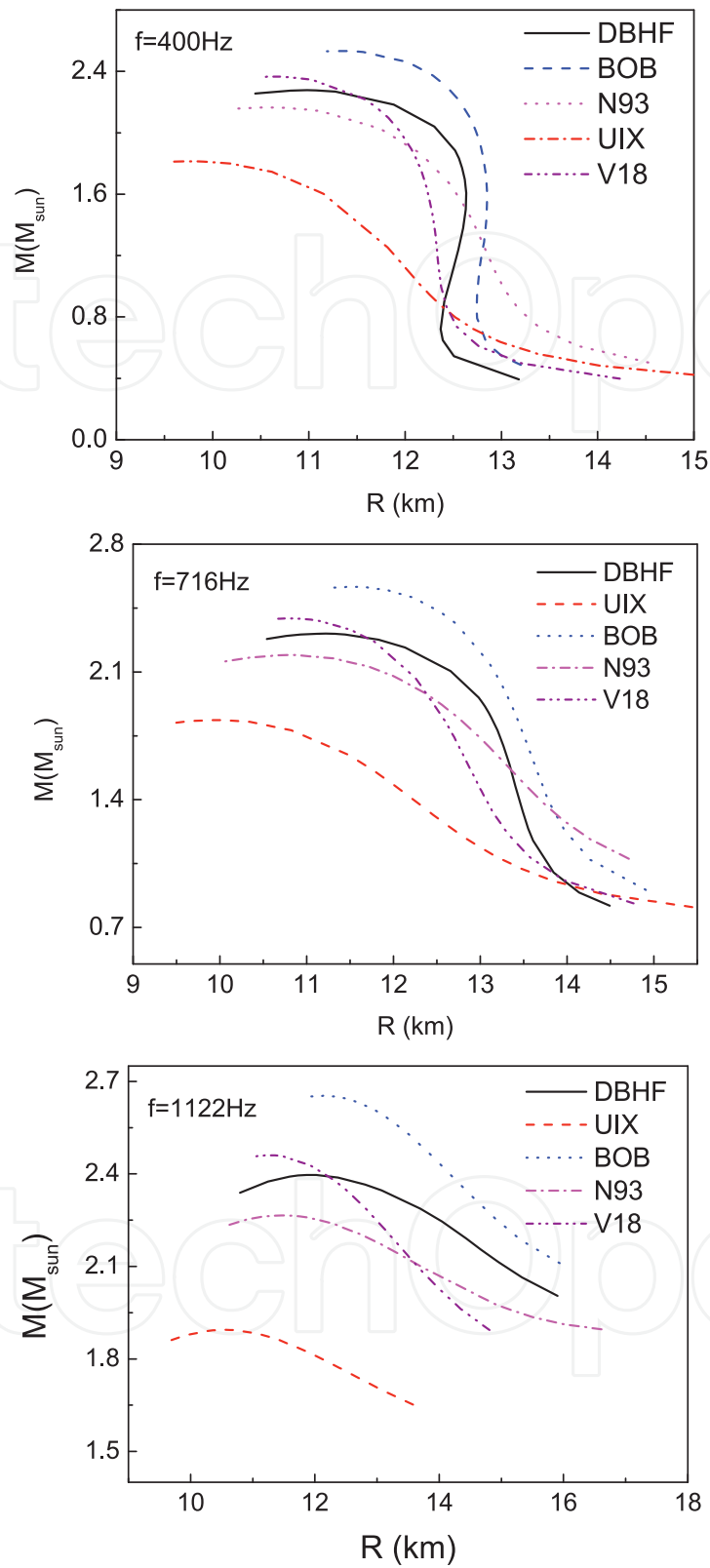
Fig. 18. Mass-radius relation for the models considered in the text and for different rotational frequencies.
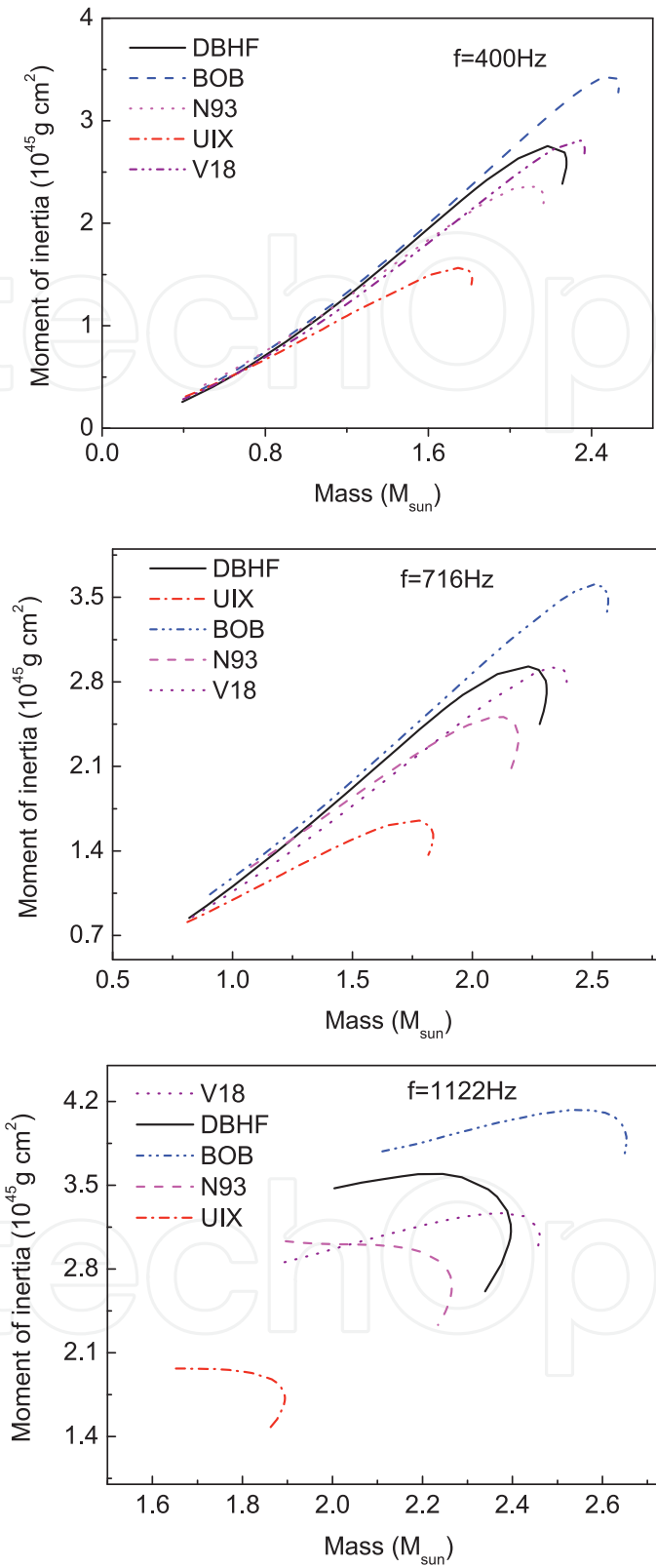
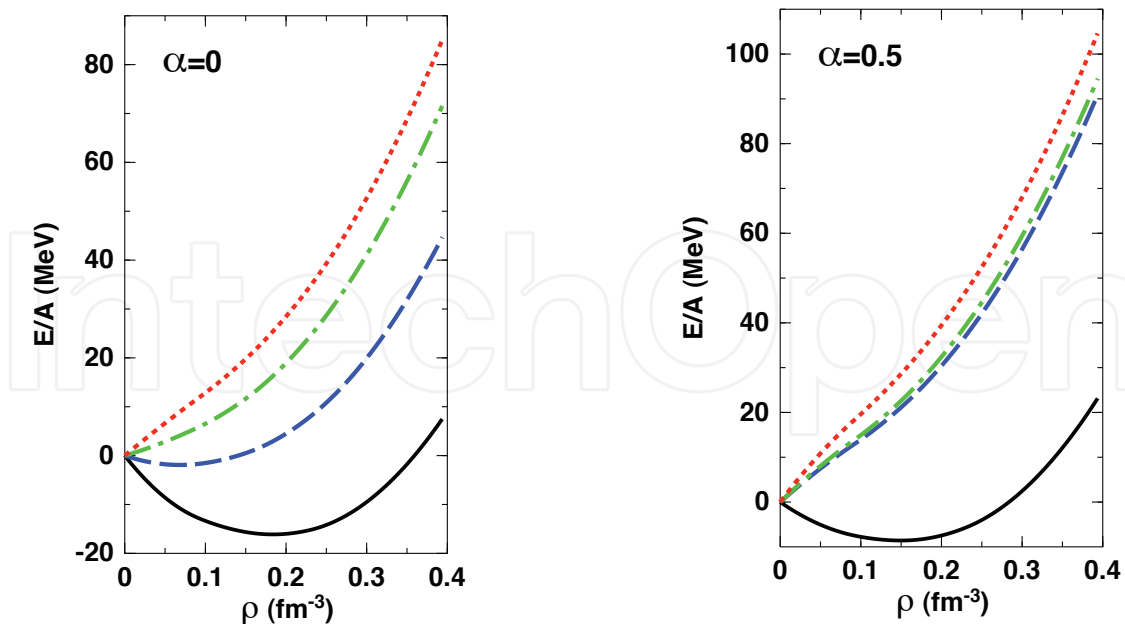Fig. 19. Moment of inertia for the models considered in the text and for different rotational frequencies.

Fig. 20. The energy per particle as a function of density and variuos degrees of proton and neutron polarizations in symmetric matter (left) and asymmetric matter (right). In both frames, the (blue) dashed line corresponds to totally polarized neutrons and unpolarized protons (β_n=1, β_p=0); the (green) dash-dotted line is the prediction for the FM state (β_n=1, β_p=1); the (red) dotted line shows the energy of the AFM state (β_n=1, β_p=-1). The (black) solid line shows the predictions for unpolarized matter.

being the most energetic. Thus, a phase transition to a spin-ordered state is not anticipated in our model. This conclusion seems to be shared by predictions of microscopic models, such as those based on conventional Brueckner-Hartree-Fock theory (Vidaña & Bombaci, 2002). On the other hand, calculations based on various parametrizations of Skyrme forces result in different conclusions. For instance, with the *SLy4* and *SLy5* forces and the Fermi liquid formalism a phase transition to the AFM state is predicted in asymmetric matter at a critical density equal to about 2-3 times normal density (Isayev & Yang, 2004).

In closing this brief section, it is interesting to remark that models based on realistic nucleon-nucleon potentials, whether relativistic or non-relativistic, are at least in qualitative agreement with one another in predicting more energy for totally polarized states (FM or AFM) up to densities well above normal density.

6. Summary and conclusions

In this chapter, we have been concerned with the nuclear equation of state of isospin asymmetric nuclear matter, the main input for calculations of the properties of compact stars as well as a variety of other systems, such as the neutron skin of neutron-rich nuclei.

After describing our microscopic approach to the development of the equation of state for nuclear matter and neutron-rich matter, we presented a brief review of the structure equations leading to the prediction of neutron star properties. Microscopic predictions from different models employing three-body forces along with the non-relativistic Brueckner-Hartree-Fock

method have also been shown for comparison. Large model dependence is seen among predictions, especially those involving the highest densities.

Rich and diverse effort is presently going on to improve the available constraints on the EoS or find new ones. These constraints are usually extracted through the analysis of selected heavy-ion collision observables. At the same time, partnership between nuclear physics and astrophysics is becoming increasingly important towards advancing our understanding of exotic matter. The recently approved Facility for Rare Isotope Beams (FRIB), thanks to new powerful technical capabilities, will forge tighter links between the two disciplines, as it will allow access to rare isotopes which play a critical role in astrophysical processes but have not yet been observed in terrestrial laboratories.

7. Acknowledgements

8. References

Alonso, D. & Sammarruca, F. (2003). Microscopic Calculations in Asymmetric Nuclear Matter. *Phys. Rev. C* Vol. 67, 054301, pp. 1-16.

Baldo, M., Burgio, G.F. & Schulze, H.-J. (1998). Onset of Hyperon Formation in Neutron Star Matter from Brueckner Theory. *Phys. Rev. C* Vol. 58, pp. 3688-3695.

Bejger, M. & Haensel, P. (2003). Accelerated expansion of the Crab nebula and evolution of its neutron-star parameters. *Astron. Astrophys.* Vol. 405, pp. 747-752.

Bodmer, A.R. (1971). Collapsed Nuclei. *Phys. Rev. D* Vol. 4, pp. 1601-1606.

Boguta, J. (1981). Remarks on the Beta Stability in Neutron Stars. *Phys. Lett. B* Vol. 106, pp. 255-258.

Borderie, B. & Rivet, M.F. (2008). Nuclear Multifragmentation and phase transition for hot nuclei. *Prog. Part. Nucl. Phys.* Vol. 61, pp. 551-601.

Brockmann, R. & Machleidt, R. (1990). Relativistic Nuclear Structure I. Nuclear Matter. *Phys. Rev. C* Vol. 42, pp. 1965-1980.

Brown, G.E. (1979). Chiral Symmetry and the Nucleon-Nucleon Interaction, *in* Rho, M. & Wilkinson, D.H. (Ed.), *Mesons in Nuclei*, Vol. I, North-Holland, Amsterdam, pp. 330-356.

Brown, G.E., Weise, W., & Baym, G. (1987). Relativistic effects in Nuclear Physics. *Comments Nucl. Part. Phys.* Vol. 17, pp. 39-62.

Champion, D.J. et al. (2008). An eccentric Binary Millisecond Pulsar in the Galactic Plane. *Science* Vol. 320, pp. 1309-1312.

Danielewicz, P., Lacey, R. and Lynch, W.G. (2002). Determination of the equation of state of dense matter. *Science* Vol. 298, pp. 1592-1596.

Demorest, P. et al. (2010). Shapiro delay measurement of a two solar mass neutron star. *Nature* Vol. 468, pp. 1081-1083.

Faulkner, A.J. et al. (2004). A new relativistic double neutron star system. *Astrophys. J.* Vol. 618, pp. L119-L122.

Feng, Z.-Q. & Jin, G.-M. (2010). Probing the Symmetry Energy at Supra-Saturation Densities from Pion Emission in Heavy-Ion Collisions, *Proceedings of the International Workshop on Nuclear Dynamics in Heavy-Ion Reactions and the Symmetry Energy*, pp. 1686-1693, Shanghai, China, August 23-25, 2009, Special Issue of Int. J. Mod. Phys. E Vol. 19, World Scientific, Singapore.

Furnstahl, R.J. (2002). Neutron radii in mean-field models. *Nucl. Phys. A* Vol. 706, pp. 85-110.

Glendenning, N.K. (1997). *Compact Stars, Nuclear Physics, Particle Physics, and General Relativity*, Springer-Verlag, New York.

Greco, V. et al. (2010). Probing the Symmetry Energy at High Baryon Density with Heavy-Ion Collisions, *Proceedings of the International Workshop on Nuclear Dynamics in Heavy-Ion Reactions and the Symmetry Energy*, pp. 1664-1674, Shanghai, China, August 23-25, 2009, Special Issue of Int. J. Mod. Phys. E Vol. 19, World Scientific, Singapore.

Haftel, M.I. & Tabakin, F. (1970). Nuclear Saturation and the Smoothness of Nucleon-Nucleon Potentials. *Nucl. Phys. A* Vol. 158, pp. 1-42.

Harrison, B.K., Thorne, K.S., Wakano, M., and Wheeler, J.A. (1965). *Gravitation Theory and Gravitational Collapse*, University of Chicago Press, Chicago.

Hessels, J.W.T. et al. (2006). A radio pulsar spinning at 716-Hz. *Science* Vol. 311, pp. 1901-1904.

Isayev, A.A. & Yang, J. (2004). Antiferromagnetic spin phase transition in nuclear matter with effective Gogny interaction. *Phys. Rev. C* Vol. 70, 064310, pp. 1-6.

Isobe, T. (2011). Overview of SAMURAI/TPC Project. Talk presented at the International Symposium on Nuclear Symmetry Energy, Smith College, June 17-20, 2011.

Kaaret, P. et al. (2006). Discovery of 1122-Hz X-Ray Burst Oscillations from the Neutron Star X-Ray Transient XTE J1739-285. arXiv:0611716 [astro-ph].

Klähn, T. et al. (2006). Constraints on the high-density nuclear equation of state from the phenomenology of compact stars and heavy-ion collisions. *Phys. Rev. C* Vol. 74, 035802, pp. 1-15.

Ko, C.M. et al. (2010). Medium Effects on Charged Pion Ratio in Heavy Ion Collisions. *Proceedings of the International Workshop on Nuclear Dynamics in Heavy-Ion Reactions and the Symmetry Energy*, pp. 1763-1772, Shanghai, China, August 23-25, 2009, Special Issue of Int. J. Mod. Phys. E Vol. 19, World Scientific, Singapore.

Kohley, Z. et al. (2011). Transverse collective flow and midrapidity emission of isotopically identified light charged particles. *Phys. Rev. C* Vol. 83, 044601, pp. 1-10.

Lane, A.M. (1962). Isobaric spin dependence of the optical potential and quasi-elastic (p,n) reactions. *Nucl. Phys.* Vol. 35, p. 676-685.

Lattimer, J.M. & Prakash, M. (2007). Neutron star observations: Prognosis for equation of state constraints. *Phys. Rep.* Vol. 442, pp. 109-165.

Li, B.-A. & Chen, L.-W. (2005). Nucleon-nucleon cross sections in neutron-rich matter and isospin transport in heavy-ion reactions at intermediate energies. *Phys. Rev. C* Vol. 72, 064611, pp. 1-12.

Li, Z.H. et al. (2008). Consistent nucleon-nucleon potentials and three-body forces. *Phys. Rev. C* Vol. 77, p. 034316 (1-10).

Li, Z.H. & Schulze, H.-J. (2008). Neutron star structure with modern nucleonic three-body forces. *Phys. Rev. C* Vol. 78, 028801, pp. 1-4.

Machleidt, R. (1989). The meson theory of nuclear forces and nuclear structure, *in* Negele, J.W. & Vogt, E. (ed.), *Adv. Nucl. Phys.*, Plenum Press, New York, Vol. 19, pp. 189-376.

Machleidt, R. (2001). High-precision, charge-dependent Bonn nucleon-nucleon potential. *Phys. Rev. C* Vol. 63, 024001, pp. 1-32.

Negele, J.W. & Vautherin, D. (1973). Neutron star matter at subnuclear densities. *Nucl. Phys. A* Vol. 207, pp. 298-320.

Nice, D.J. et al. (2005). A 2.1 solar mass pulsar measured by relativistic orbital decay. *Astrophys. J.* Vol. 634, pp. 1242-1249.

Oyamatsu, K., Tanihata, I., Sugahara, Y., Sumiyoshi, K., & Toki, H. (1998). Can the equation of state of asymmetric nuclear matter be studied using unstable nuclei? *Nucl. Phys. A* Vol. 634, p. 3-14.

Pieper, S.C., Pandharipande, V.R., Wiringa, R.B., & Carlson, J. (2001). Realistic models of pion-exchange three-nucleon interactions. *Phys. Rev. C* Vol. 64, 014001, pp. 1-21.

Rhoades, C.D. & Ruffini, R. (1974). Maximum mass of a neutron star. *Phys. Rev. Lett.* Vol. 32, pp. 324-327.

Salpeter, E.E. & Bethe, H.A. (1951). A Relativistic Equation for Bound-State Problems. *Phys. Rev.* Vol. 84, pp. 1232-1242.

Sammarruca, F. & Liu, P. (2009). Neutron skin of ^{208}Pb and density dependence of the symmetry energy. *Phys. Rev. C* Vol. 79, 057301, pp. 1-4.

Sammarruca, F. (2010). The microscopic approach to nuclear matter and neutron star matter. *Int. J. Mod. Phys. E* Vol. 19, pp. 1259-1313.

Sammarruca, F. (2011). Spin- and isospin-polarized states of nuclear matter in the Dirac-Brueckner-Hartree-Fock model. *Phys. Rev. C* Vol. 83, p. 064304 (1-6).

Sammarruca, F. (2011). Contribution of isovector mesons to the symmetry energy in a microscopic model. arXiv:1107.3339 [nucl-th].

Schulze, H.-J., Polls, A., Ramos, A., & Vidaña, I. (2006). Maximum mass of neutron stars. *Phys. Rev. C* Vol. 73 058801, pp. 1-4.

Sedrakian, A. (2007). The physics of dense hadronic matter and compact stars. *Prog. Part. Nucl. Phys.* Vol. 58, pp. 168-246.

Sfienti, C. *et al.* (2009). Isotopic Dependence of the Nuclear Caloric Curve. *Phys. Rev. Lett.* Vol. 102, 152701, pp. 1-4.

Simenel, C., Chomaz, Ph., & de France, G. (2007). Fusion process with a preequilibrium giant dipole resonance in time-dependent Hartree-Fock theory. *Phys. Rev. C* Vol. 76, 024609, pp. 1-14.

Stocks, V.G.J., Klomp, R.A.M., Terheggen, C.P.F., & de Swart, J.J. (1994). Construction of high-quality NN potential models. *Phys. Rev. C* Vol. 49, pp. 2950-2962.

Terazawa, H. (1989). Superhypernuclei in the Quark Shell Model. *J. Phys. Soc. Japan* Vol. 58, pp. 3555-3563.

Thompson, R.H. (1970). Three-Dimensional Bethe-Salpeter Equation Applied to the Nucleon-Nucleon Interaction. *Phys. Rev. D* Vol. 1, pp. 110-117.

Trautmann, W. et al. (2009). Neutron-proton elliptic flow in Au+Au. arXiv:0907.2822 [nucl-ex].

Tsang, M.B. et al. (2009). Constraints on the density dependence of the symmetry energy. *Phys. Rev. Lett.* Vol. 102, 122701, pp. 1-12.

Vidaña, I. & Bombaci, I. (2002). Equation of state and magnetic susceptibility of spin polarized isospin asymmetric nuclear matter. *Phys. Rev. C* Vol. 66, 045801, pp. 1-11.

Weber, F. (1999). *Pulsars as Astrophysical Laboratories for Nuclear and Particle Physics*, Institute of Physics Publishing, Bristol and Philadelphia.

Weinberg, S. (1990). Nuclear forces from chiral Lagrangians. *Phys. Lett. B* Vol. 251, pp. 288-292.

Wiringa, R.B., Stocks, V.G.J., & Schiavilla, R. (1995). Accurate nucleon-nucleon potential with charge-independence breaking. *Phys. Rev. C* Vol. 51, pp. 38-51.

Witten, E. (1984). Cosmic separation of phases. *Phys. Rev. D* Vol. 30, pp. 272-284.

Xu, C., Li, B.-A., & Chen, L.-W. (2010). Symmetry energy, its density slope, and neutron-proton effective mass splitting at normal density extracted from global nucleon optical potentials. *Phys. Rev. C* Vol. 82, 054607, pp. 1-5.

Yong, G.-C., Li, B.-A., & Chen, L.-W. (2010). Triton-^{3}HE Relative and Differential Flows and the High Density Behavior of Nuclear Symmetry Energy. *Proceedings of the International Workshop on Nuclear Dynamics in Heavy-Ion Reactions and the Symmetry Energy*, pp. 1647-1652, Shanghai, China, August 23-25, 2009, Special Issue of Int. J. Mod. Phys. E Vol. 19, World Scientific, Singapore.
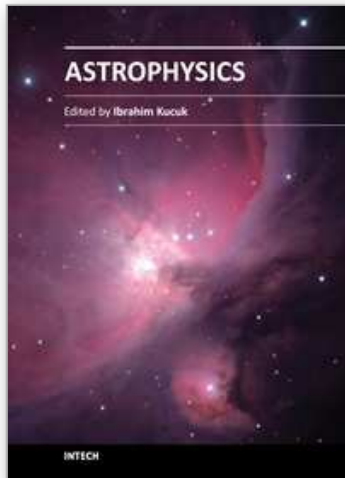
Astrophysics

Edited by Prof. Ibrahim Kucuk

This book provides readers with a clear progress to theoretical and observational astrophysics. It is not surprising that astrophysics is continually growing because very sophisticated telescopes are being developed and they bring the universe closer and make it accessible. Astrophysics Book presents a unique opportunity for readers to demonstrate processes do occur in Nature. The unique feature of this book is to cover different aspects in astrophysics covering the topics: • Astronomy • Theoretical Astrophysics • Observational Astrophysics • Cosmology • The Solar System • Stars • Planets • Galaxies • Observation • Spectroscopy • Dark Matter • Neutron Stars • High Energy Astrophysics

How to reference

In order to correctly reference this scholarly work, feel free to copy and paste the following:

Francesca Sammarruca (2012). A Microscopic Equation of State for Neutron-Rich Matter and Its Effect on Neutron Star Properties, Astrophysics, Prof. Ibrahim Kucuk (Ed.), ISBN: 978-953-51-0473-5, InTech, Available from: http://www.intechopen.com/books/astrophysics/neutron-star-properties-and-the-nuclear-equation-of-state

INTECH
open science | open minds